

1 **Measurement report: Assessing the ammonia characteristics over a**
2 **high-altitude mountain site in Shanxi province, China: a comparison**
3 **with the observations in the North China Plain**

4
5 Weiwei Pu ^{a,b}, Jing Xu ^{a,b*}, Lingyun Zhu ^c, Chao Liu ^{a,b}, Liyan Zhou ^{a,b}, Jian Dong^d,
6 Shuangshuang Ge ^{a,b}, Zhiqiang Ma ^{a,b*}

7
8 ^a Institute of Urban Meteorology, China Meteorological Administration, Beijing 100089, China

9 ^b Beijing Shangdianzi Regional Atmosphere Watch Station, Beijing 101507, China

10 ^c Shanxi Institute of Meteorological Science, Shanxi Center of Technology Innovation for
11 Environmental Meteorology Forecast and Evaluation, Taiyuan 030002, China

12 ^d Shanxi Wutaishan Meteorological Station, Xinzhou 035515, China

13
14
15 **Abstract:**

16 Ammonia (NH₃) acts as the dominant alkaline gas and plays a crucial role in
17 atmospheric chemistry, thereby influencing air quality and ecological systems. Previous
18 NH₃ measurement studies have primarily focused on near-ground environments or
19 relied on passive sampling methods; however, continuous, high-resolution NH₃
20 observations at high-altitude sites remain scarce. This study investigated NH₃
21 characteristics at a high-altitude mountain site (WTM) in northern China, using high-
22 resolution and real-time measurement data spanning a full annual cycle. It also
23 compared a regional background site (SDZ) with an urban site (BMS) to better
24 understand the regional features of NH₃ in northern China. A multi-method approach
25 was employed, integrating in situ NH₃ measurements, meteorological data analyses,
26 Convergent Cross Mapping (CCM), Potential Source Contribution Function (PSCF),
27 and WRF-Chem modeling, to identify NH₃ source regions and clarify underlying
28 transport mechanisms. The results indicated that NH₃ emissions from the North China
29 Plain (NCP) can reach WTM and SDZ through distinct circulation patterns: mountain-
30 plain circulations for WTM, and primary mountain-valley circulations for SDZ.
31 Notably, despite significant differences in altitude, geography, and pollutant transport

* Corresponding author at: Institute of Urban Meteorology, China Meteorological Administration, Beijing 100089, China.
E-mail address: jxu07@126.com; zqma@ium.cn

32 mechanisms between WTM and SDZ, regional agricultural emissions in the NCP were
33 the dominant factor driving the similarity in NH₃ levels at the two sites. This study
34 enhances the understanding of how surface emissions influence NH₃ concentrations at
35 high-altitude mountain site and highlights the critical role of NCP emissions in
36 influencing regional NH₃ levels, thereby providing insights for formulating strategies
37 to mitigate regional NH₃ pollution.

38 **Keywords:** ammonia, high-altitude mountain site, background station, Convergence
39 Cross Mapping (CCM), transport mechanism

40

41 1. Introduction

42 Ammonia (NH₃) mainly comes from fertilizers and animals, and other sources
43 include industry, fossil fuels, crops, soils, oceans, and biomass burning (Warner et al.,
44 2017; Warner et al., 2015). As the most important gas-phase alkaline species, NH₃
45 contributes considerably to the formation and development of fine particles (PM_{2.5}),
46 which have implications for human health, degrade regional air quality, and influence
47 the global radiation budgets. However, NH₃ emission control would mitigate nitrogen
48 deposition and haze pollution but worsen acid rain (Liu et al., 2019). The atmospheric
49 lifetime of NH₃ ranges from hours to days, depending on factors like deposition
50 processes and the presence of other reactive species (Baek et al., 2004); the global
51 average atmospheric lifetime is about 11 h (Xu et al., 2012).

52 Due to its short lifetime, NH₃ is highly concentrated in the planetary boundary
53 layer and near emission sources. Therefore, most of the current NH₃ measurements
54 were implemented at near-surface sites (Pu et al., 2023; Kuang et al., 2020; Zhang et
55 al., 2023; Elser et al., 2018). However, aircraft measurements revealed there were NH₃
56 pollution layers, where the concentrations were comparable to that of the surface,
57 within the lower free troposphere (FT) over the North China Plain (NCP) (Pu et al.,
58 2020a). Aircraft-borne campaign measurements over the US obtained concentration
59 profiles in the FT reaching altitudes of about 6 km (Nowak et al., 2007; Nowak et al.,
60 2010; Nowak et al., 2012; Leen et al., 2013; Schiferl et al., 2016). Although aircraft
61 could capture the vertical distribution of NH₃ in FT, only for the limited durations of

62 measurement campaigns. Satellite NH₃ observations complement current ground and
63 airborne measurements by providing unique insights on NH₃ distributions from
64 regional to global scales, such as the Tropospheric Emission Spectrometer (TES)
65 instrument on the NASA Aura satellite (Shephard et al., 2011), the Infrared
66 Atmospheric Sounding Interferometer (IASI) instrument on the MetOp-A and MetOp-
67 B satellites (Van Damme et al., 2014), and the Cross-track Infrared Sounder (CrIS)
68 instrument on the NASA satellite (Dammers et al., 2019). However, the vertical
69 sensitivity of these satellite retrievals is mainly limited to the lower troposphere up to
70 approximately 3 km, and no altitude resolution is achieved (Höpfner et al., 2016). These
71 findings underscore the significance of studying ammonia at high-altitude sites, where
72 its impact on large-scale pollution may be even more pronounced.

73 High-altitude mountain sites have long been recognized as suitable places for
74 characterizing the chemical composition of the lower troposphere. These sites allow for
75 measurements that are representative of continental to hemispheric scales by focusing
76 on air masses that have travelled far from emission sources and had sufficient time to
77 mix. Although NH₃ concentration observations have been conducted at mountain sites
78 in previous studies, the relevant data remain relatively limited. Among these,
79 continuous observation data with high-resolution is particularly scarce. Such
80 continuous measurements offer an opportunity to establish connections between NH₃
81 concentrations and the dynamic changes in source emissions as well as transport
82 patterns.

83 To improve our understanding of the characteristics and influencing factors of NH₃
84 in the lower FT, a one-year measurement was conducted at a high-altitude mountain
85 site (Mountain Wutai, WTM) in northern China. Because WTM is located to the west
86 of the NCP, one of the NH₃ high-emission regions in the world (Van Damme et al.,
87 2018), it provides an opportunity to compare its patterns with those of other sites within
88 the NCP. Overall, the primary goals of this work were to characterize NH₃ levels at
89 WTM and other sites in NCP and to further interpret the similarities or different
90 transport patterns between these sites.

91

92 **2. Experimental and Methods**

93 **2.1. Experimental site and Instrument**

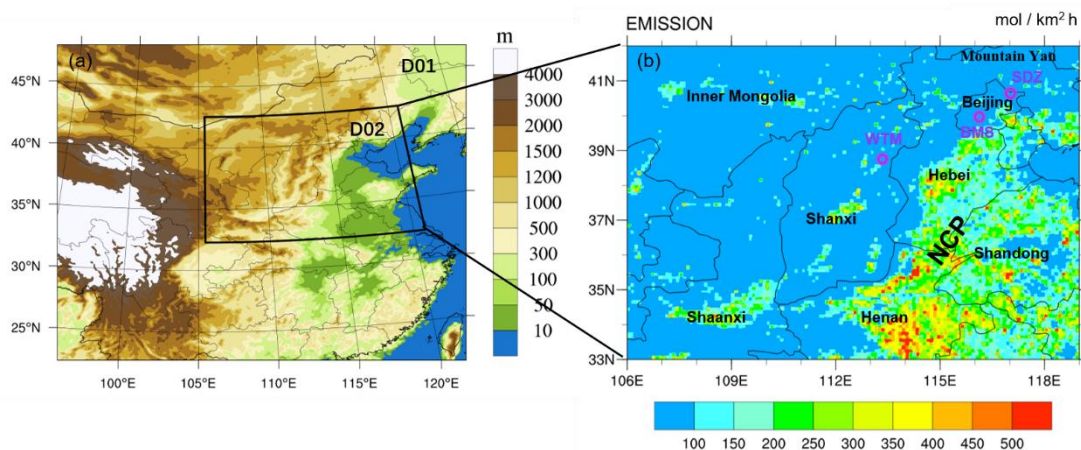
94 From June 2020 to May 2021, continuous in situ measurements were carried out
95 at a mountain site in Shanxi province, a background site and an urban site in Beijing.
96 The mountain site, Mountain Wutai (WTM; 38.95 °N, 113.52 °E; 2208 m a.s.l.) is
97 located in the northeast Shanxi province (Fig.1), which is connected to the continental
98 plateau extending to the west. Due to its high altitude and remote location, there are no
99 major pollution sources, making it an appropriate site for characterizing lower FT NH₃.
100 The fluctuations in the hourly and daily average for temperature (T), relative humidity
101 (RH), wind direction (WD), wind speed (WS), and precipitation, are depicted in Fig.S1.
102 The annual average T, RH, and total precipitation are 2.5 °C, 62.6 %, and 892.7 mm,
103 respectively. Prevailing winds are generally westerly, with an average speed of 5.8 m/s.

104 The background site, Shangdianzi (SDZ; 40.65°N, 117.11°E; 293.9 m a.s.l.), lies
105 in the transitional region between the NCP and the Mountain Yan area (Fig. 1). It acts
106 as both a regional background station in China and a regional site under the Global
107 Atmosphere Watch program. The mountainous areas around the SDZ station only
108 contain small villages, where populations are sparse and anthropogenic emission
109 sources are negligible. Therefore, the station's atmospheric pollution levels can
110 represent the background concentration of air pollutants in North China. Nevertheless,
111 orchards surrounding SDZ may have ammonium dibasic phosphate and urea applied as
112 soil fertilizers during spring.

113 The urban site is situated at the Beijing Meteorological Service (BMS; 39.93°N,
114 116.27°E; 90 m a.s.l.) (Fig. 1), which lies in the northwestern sector of the Beijing urban
115 area, surrounded by various land use types (commercial areas, park, residential areas,
116 and traffic areas).

117 Real-time NH₃ concentrations at the above-mentioned stations were measured
118 using three analyzers (907, Los Gatos Research Inc., US). To ensure data accuracy and
119 reliability, rigorous quality assurance (QA) and quality control (QC) procedures,

120 including daily zero and span checks, monthly multi-point calibrations using certified
 121 NH₃ standard gas, were implemented throughout the campaign. Other than NH₃
 122 observations, methane (CH₄) was also measured at SDZ by a Picarro G2401
 123 CO₂/CO/CH₄ cavity-ringdown spectrometer during summer 2020 and spring 2021.
 124 Meteorological data of the surface in this study were achieved from the China
 125 Meteorological Data Service Center (<http://data.cma.cn/en>). The planetary boundary
 126 layer height (BLH) and U, V, and W winds are achieved from the ERA5
 127 (<https://cds.climate.copernicus.eu/datasets>), a fifth-generation European Centre for
 128 Medium-Range Weather Forecasts (ECMWF) reanalysis data with a spatial resolution
 129 of 0.25°×0.25°.



130
 131 Fig. 1. Simulation domains and topographic distribution (a); spatial distribution of NH₃ emission
 132 intensity and locations of the measurement sites (indicated by purple open circles) (b).

133 2.2. Convergence cross mapping (CCM) method

134 Given the complex interactions in atmospheric environments and the strong
 135 nonlinearity of atmospheric systems, simple correlation analyses (e.g., Pearson
 136 correlation, which is only applicable to linear systems) cannot effectively quantify the
 137 causal effects of individual meteorological factors on NH₃ concentrations. To address
 138 this limitation, Sugihara et al. (2012) developed Convergent Cross Mapping (CCM) —
 139 a robust causal analysis approach—designed to extract the coupling relationships
 140 between individual variables in complex systems. This method serves as a suitable
 141 alternative for identifying nonlinear associations within the same system and evaluating
 142 weak-to-moderate coupling effects, while also enabling the determination of interaction

143 directionality. Therefore, it has been widely adopted in related studies.

144 In CCM, the predictive skill of variable A for variable B is calculated and denoted
145 as ρ (ranging from 0 to 1). This metric provides a quantitative basis for comparing the
146 influence magnitudes of different variables on a target variable. Detailed descriptions
147 of the CCM algorithm have been published in previous literature (Chen et al., 2022;
148 Ziyue et al., 2018; Rawat et al., 2024). The CCM analysis in this study was conducted
149 using R software (version 4.3.1), with the support of the rEDM package (Sugihara et
150 al., 2012) and the multispatialCCM package (Clark et al., 2015).

151 **2.3. Potential source contribution function (PSCF)**

152 To identify the locations of sources influencing different pollutant concentrations,
153 PSCF analysis was applied, with its calculation relying on measured concentrations and
154 associated trajectory data. A high PSCF value denotes that the corresponding region
155 transports substantial amounts of the target atmospheric pollutant to the receptor site.
156 In contrast, a low PSCF value may reflect either minimal emissions from the region or
157 the absence of pollutant transport pathways from that region to the receptor site.

158 From June 2020 to May 2021, 48-hour backward trajectories were calculated 24
159 times per day (00:00 to 23:00 UTC, with initiation at 10 m above ground surface) using
160 the HYSPLIT model developed by the National Oceanic and Atmospheric
161 Administration Air Resource Lab (NOAA;
162 <http://www.arl.noaa.gov/ready/hysplit4.html>). Meteorological input data were derived
163 from the FNL global analysis data—generated by the National Center for
164 Environmental Prediction (NCEP) model and processed by the Global Data
165 Assimilation System (GDAS) with a spatial resolution of $1^\circ \times 1^\circ$
166 (<http://www.rl.noaa.gov/ss/transport/archives.hrml>). Detailed methodologies for the
167 PSCF approach and weighted potential source contribution function (WPSCF) analysis
168 have been reported in previous studies (Wang, 2014; Pu et al., 2019). The 70th percentile
169 of NH₃ concentrations over the entire observation period was used as the criterion value.

170 **2.4. WRF-Chem**

171 The WRF-Chem model (version 4.2.1) was employed to simulate NH₃

172 concentrations and meteorological conditions in this study. A detailed description of
173 WRF-Chem is provided by Grell et al. (2005). The model uses the CBM-Z gas phase
174 chemical mechanism (Zaveri and Peters, 1999) to represent the transformation
175 reactions of NH_3 in the atmosphere.

176 In this study, two nested domains with horizontal resolutions of 9 km and 3 km
177 were established within the WRF-Chem model, centered at 116°E , 39°N (Fig. 1). The
178 inner domain (D02, shown in Fig. 1a) covers the primary agricultural region of the
179 North China Plain, which includes three major crop-producing provinces: Henan, Hebei,
180 and Shandong. In the vertical direction, the model was configured with 30 sigma-
181 pressure layers extending from the surface up to 50 hPa, 12 of which are located within
182 the atmospheric boundary layer. Meteorological initial and boundary conditions were
183 derived from the NCEP Final Operational Global Analysis (FNL) dataset, which has a
184 spatial resolution of $1.0^\circ \times 1.0^\circ$ and a temporal resolution of 6 hours. Anthropogenic
185 emissions were based on the inventory developed by Zhang et al. (2009), which was
186 subsequently updated to a resolution of $0.1^\circ \times 0.1^\circ$ for the year 2019 (MEIC-2019,
187 Zhang, personal communication). Biomass burning emissions were obtained from the
188 Fire Inventory from NCAR (FINNv1.5, Wiedinmyer et al., 2011). Chemical initial and
189 boundary conditions were initialized using model-default idealized profiles. The
190 simulation was conducted from May 1 to 12, 2021, with the first 11 days considered as
191 model spin-up and results from May 12, 2021, used for subsequent analysis.

192

193 **3. Results and Discussion**

194 **3.1. Overall features of NH_3 concentration**

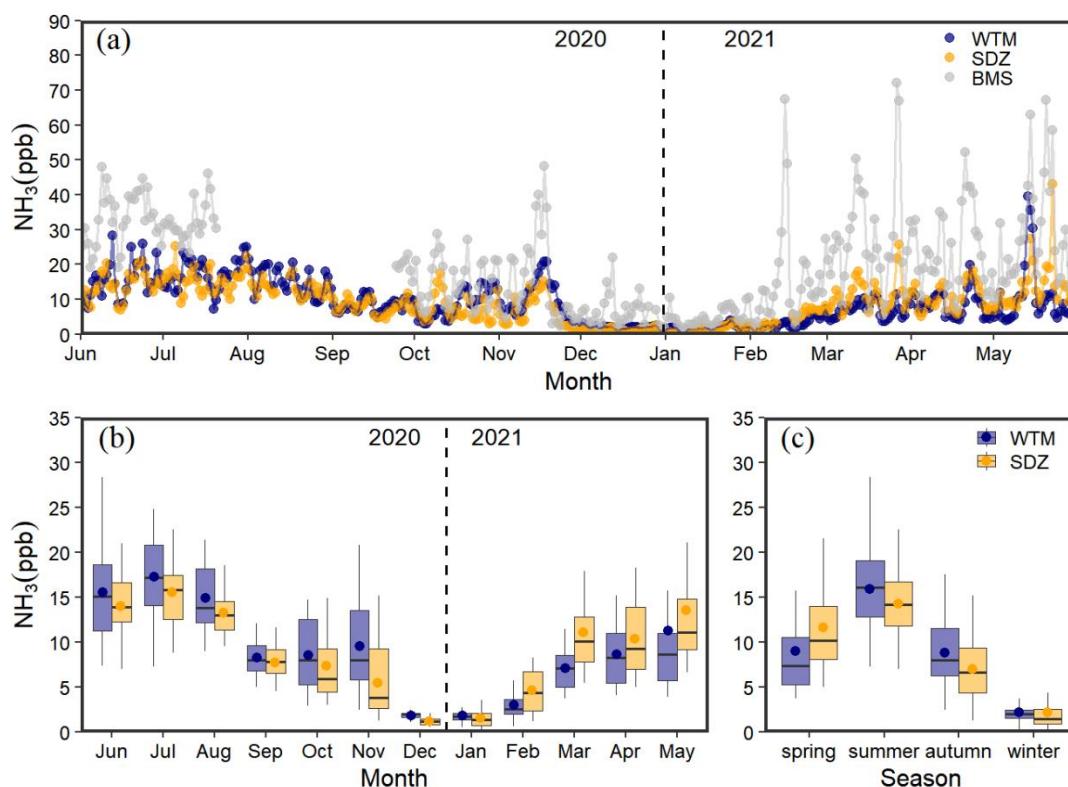
195 The continuous variability of NH_3 concentrations at WTM during 2020 and 2021
196 is shown in Fig. 2. The hourly NH_3 concentration ranged from 1 to 52.7 ppb, with a
197 year-round average of 9.0 ± 6.7 ppb. The NH_3 concentrations in this study exhibited a
198 seasonal variation (Table S1), with means of 8.9 ± 6.3 , 15.9 ± 5.4 , 8.8 ± 4.2 , and $2.1 \pm$
199 1.2 ppb in spring, summer, autumn, and winter, respectively. Compared with other high-
200 altitude sites (Table S2), the average concentration of NH_3 at WTM is obviously higher

201 than most of the sites, particularly at Rocky Mountain National Park, Beaver Meadows,
202 Timber Creek, and Gore Pass in the USA and the Happo site in Japan. In contrast, NH₃
203 levels at WTM were substantially lower than those recorded at rural and agricultural
204 sites, such as Wuwei in China and Greeley and Kersey in the United States, highlighting
205 the influence of anthropogenic emissions. Notably, within the same type of observation
206 site, forest or grassland, the NH₃ concentrations measured at WTM are elevated. These
207 discrepancies imply that local sources, atmospheric transport processes, or
208 topographical factors may contribute to enhanced ammonia accumulation at this site
209 compared to similar ecological settings.

210 Situated in a remote, high-altitude area to the west of the NCP, this unique location
211 enables comparative studies between WTM and other sites located in the NCP. As can
212 be seen from Figure 2(a), the NH₃ concentration and its variation pattern at the WTM
213 site exhibit a high degree of similarity to those at the SDZ site, while showing
214 significant differences from the BMS site, where the NH₃ concentration levels are
215 notably higher. To further quantify the similarity of NH₃ variation tendency among the
216 sites, this study employed a variety of analytical methods, including Dynamic Time
217 Warping (DTW), Euclidean distance, Pearson correlation coefficient (r), Root Mean
218 Square Deviation (RMSD), and Mean Absolute Bias (MAB) (Table S3). The DTW was
219 processed in R version 4.3.1, along with the dtw R package (Giorgino, 2009). It is
220 noteworthy that despite the greater spatial straight-line distance (350 km) between the
221 SDZ and WTM sites compared to the BMS and WTM distance, as well as an altitude
222 difference of 1.9 km, the values of DTW, Euclidean distance, RMSD, and MAB
223 between WTM and SDZ are all lower than those between WTM and BMS. Meanwhile,
224 the r between WTM and SDZ is significantly higher than that between WTM and other
225 sites. These comprehensive quantitative analysis results fully demonstrate a high degree
226 of consistency in the variation trends and numerical distributions of the NH₃
227 concentration time series at the WTM and SDZ sites.

228 Since WTM is in a remote area, emission sources in its vicinity are relatively
229 scarce. In contrast, the BMS site is located in an urban area, with obvious emission

230 sources such as vehicle exhaust emissions (Pu et al., 2023) and residential emissions.
 231 These complex local emission sources significantly influence the NH_3 concentration
 232 level and its variation pattern at this site, leading to distinct differences from the WTM.
 233 Interestingly, despite considerable altitude and spatial separation between WTM and
 234 SDZ, they exhibited similar NH_3 variation characteristics and close concentration. The
 235 subsequent sections will conduct analyses from meteorological effects, potential source
 236 regions, and transport patterns to illustrate the primary factors driving this similarity.



237
 238 Fig. 2. Daily (a), monthly (b) and seasonal (c) variation of NH_3 concentration from Jun 1, 2020 to
 239 May 31, 2021. The solid dots represent the mean values, the horizontal lines in the box denote the
 240 median, the limits of the boxes correspond to the 25th and 75th percentiles, and the whiskers of the
 241 boxes are the 10th and 90th percentiles (b, c).

242 3.2. Effects of meteorological factors

243 Local meteorological conditions exert a significant impact on the NH_3 levels
 244 (Zhang et al., 2018). Given the complex interactions within atmospheric environments,
 245 it remains challenging to quantify how individual meteorological factors affect local
 246 NH_3 concentrations. In order to solve this problem, CCM was employed to examine the
 247 coupling relationships between these factors and NH_3 . The CCM analysis based on

248 hourly data is shown in Table 1, and the influence of local meteorological factors —
249 including WS, WD, T, RH, pressure (P), and BLH — on NH₃ in different seasons is
250 determined. The convergent cross maps were used to explain the quantitative coupling
251 between NH₃ concentration and each individual meteorological factor (Fig. S2). The ρ
252 -value from CCM methods is designed to understand the coupling between two
253 variables by excluding influences from other factors. Nevertheless, it lacks the ability
254 to directly identify the positive or negative nature of the causality between the two
255 variables.

256 CCM analysis reveals that RH and T are found to show strong influence on WTM
257 NH₃ during summer, while RH and T are also found to have strong effect on SDZ NH₃
258 during spring. However, high NH₃ levels are generally associated with high temperature
259 and humidity (Lan et al., 2021). P shows a strong impact on NH₃ concentrations of
260 WTM and SDZ NH₃ in autumn and spring, respectively. That could be attributed to P
261 mainly affecting the transport and accumulation of pollutants by indirectly influencing
262 other meteorological factors (e.g., wind and humidity) (Chen et al., 2020). Although
263 various meteorological parameters affect NH₃ concentrations differently across seasons
264 at different sites, WS, WD, and BLH significantly impact NH₃ concentrations at both
265 WTM and SDZ year-round (Table 1). This indicates that wind-driven processes (e.g.,
266 atmospheric transport or dispersion) along with the boundary layer variation play
267 crucial roles in governing NH₃ levels at these sites throughout the year.

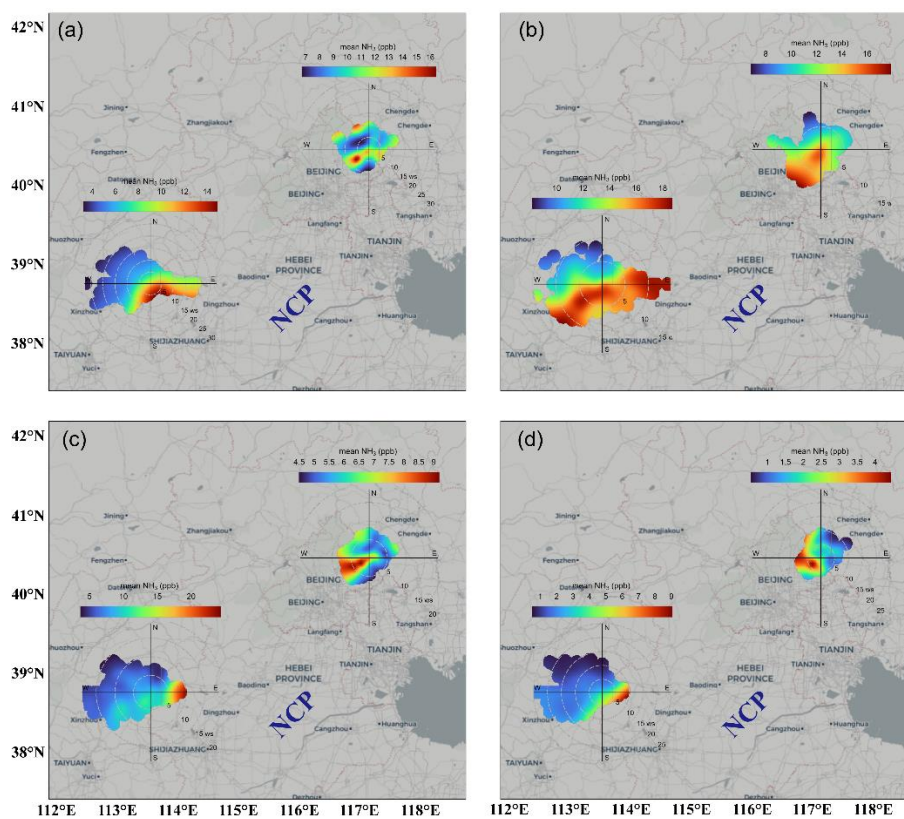
268 A bivariate polar plot is presented in Fig. 3 to analyze the function of WS and WD
269 in each season. Despite the prevailing wind being westerly (Fig. S1), the higher NH₃
270 concentrations at WTM were observed in the southeast and southwest sectors in spring
271 and summer, while elevated levels mainly occurred in the easterly direction during
272 autumn and winter. In spring and summer, the higher concentrations were accompanied
273 by a wide range of WS between 0 and 15 m/s, suggesting that local emissions and air
274 masses transported from intense NH₃ emission regions (Fig. 1b) were important factors
275 affecting NH₃ concentrations at WTM during warm seasons. However, in autumn and
276 winter, higher NH₃ concentrations were detected with a WS of 5 – 10 m/s, indicating

277 that WTM was mainly under the influence of long-distance transport during cold
 278 seasons. Unlike WTM, higher SDZ NH₃ concentrations were mainly concentrated in
 279 the southwest direction. Based on NH₃ concentration variations and WS in each season
 280 at SDZ, the site was affected by both local emissions and air mass transport.
 281 Nevertheless, the impact of transport on NH₃ was more significant, as elevated
 282 concentrations corresponded to WS exceeding 2 m/s. Notably, the NCP is located to the
 283 southeast of WTM and to the southwest of SDZ – directions that directly correspond to
 284 the WD associated with higher levels at both sites. This spatial alignment strongly
 285 suggests that the NCP might act as a potential emission area for both WTM and SDZ.

286 Table 1 Seasonal correlations and causal relationships between individual meteorological
 287 parameters and NH₃ concentration.

Site	Spring	Summer	Autumn	Winter
WTM	WS (0.42, 0.00**)	WS (0.15, 0.00**)	WS (0.46, 0.00**)	WS (0.46, 0.00**)
	WD (0.38, 0.01**)	WD (0.14, 0.00**)	WD (0.33, 0.00**)	WD (0.39, 0.00**)
	BLH (0.33, 0.00**)	T (0.22, 0.00**)	P (0.35, 0.00**)	RH (0.33, 0.00**)
		RH (0.63, 0.03*)	BLH (0.25, 0.01*)	BLH (0.20, 0.01*)
		BLH (0.23, 0.04*)		
SDZ	WS (0.31, 0.00**)	WS (0.24, 0.00**)	WS (0.36, 0.00**)	WS (0.16, 0.00**)
	WD (0.12, 0.00**)	WD (0.13, 0.02*)	WD (0.35, 0.00**)	WD (0.26, 0.00**)
	T (0.26, 0.01*)	T (0.24, 0.00**)	BLH (0.1, 0.01*)	RH (0.34, 0.00**)
	RH (0.62, 0.02*)	BLH (0.19, 0.02*)		BLH (0.21, 0.00**)
	P (0.28, 0.03*)			
	BLH (0.19, 0.00**)			

288 The causality of different meteorological factors on NH₃ is presented predictive skill (ρ) from the
 289 CCM method with p-values (p). * and ** denote the p less than 0.05 and 0.01, respectively.



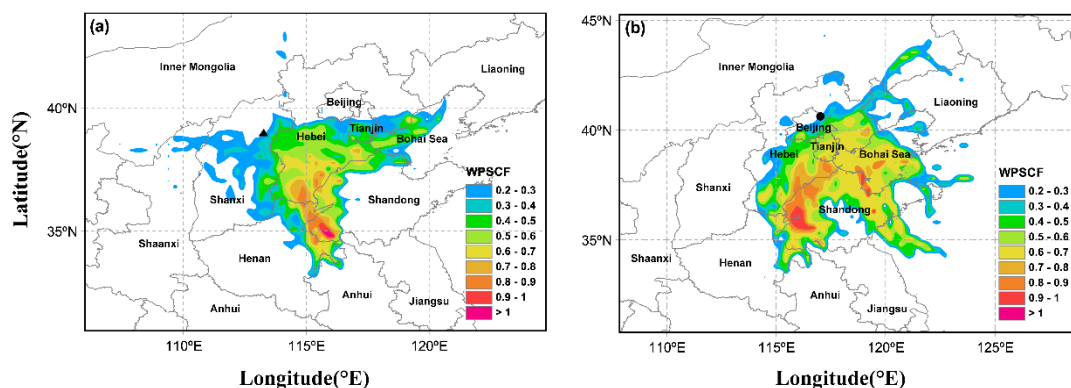
290

291 Fig. 3. Bivariate polar plots of NH₃ concentrations at WTM and SDZ in four seasons (a: spring, b:
292 summer, c: autumn, and d: winter).

293 3.3. Potential sources identified

294 To confirm whether NCP was a potential emission area for WTM and SDZ, PSCF
295 analysis was performed. The PSCF map distributions of WTM and SDZ during the
296 study period and each season are examined (Fig. 4 and Fig. S3). Grid cells characterized
297 by high PSCF values (i.e., > 0.7) were identified as regions with a high likelihood of
298 being NH₃ source areas for the receptor sites. Fig. 3 indicates that the potential sources
299 for WTM and SDZ were primarily in the broader NCP, particularly in southern Hebei,
300 western Shandong, and eastern Henan. Importantly, these locations corresponded with
301 the NH₃ emission distribution in the NCP, as shown in Fig. 1b. This region is
302 characterized by elevated anthropogenic emissions of NH₃, largely from agricultural
303 activities (Li et al., 2021). In addition to NCP, SDZ was also affected by emissions from
304 the Bohai Sea. This might be attributed to the ocean-going vessels that installed the
305 marine selective catalytic reduction technology (SCR) system to reduce NO_x emissions.
306 As catalyst activity decreases over time, NH₃ slip increases (Zhang et al., 2021). In

307 spring and summer, the potential source ranges of both sites were more scattered in
 308 NCP; however, during autumn and winter, these ranges were more concentrated in the
 309 south or east of Hebei (Fig. S3). Under the impact of southerly wind, emissions
 310 originating from NCP can be transported to WTM and SDZ.



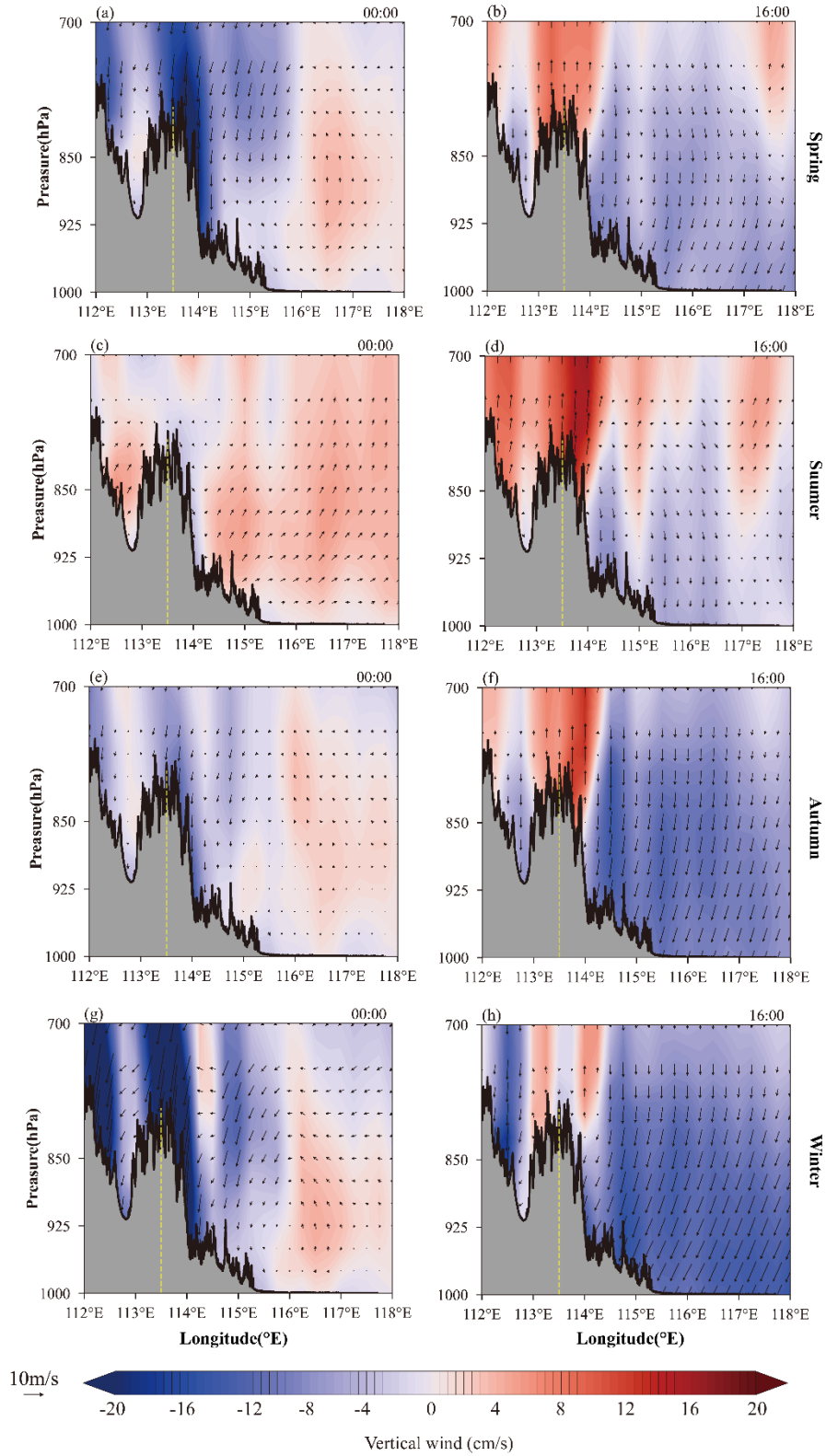
311
 312 Fig. 4. Weighted potential sources contribution analysis (PSCF) of NH_3 at WTM (a) and SDZ (b)
 313 (triangle and circle denote WTM and SDZ, respectively).

314

315 3.4. Transport patterns of NH_3

316 3.4.1. Diurnal variation of the atmospheric circulation

317 Atmospheric circulation determines the migration and transport patterns of
 318 pollutants, so to study its impact on the distribution of NH_3 concentration, the east-west
 319 cross-sections of seasonal mean wind vectors and vertical velocity were first analyzed.
 320 As shown in Fig. 5, during the daytime, low-level winds close to mountain slopes warm
 321 early, resulting in upward movement from the plain toward the mountains. At night,
 322 this pattern switches to downslope motions due to the pressure difference between
 323 mountains and plains. Therefore, although WTM is at a high altitude, local sources from
 324 NCP can still have an influence, depending largely on the vertical transport and
 325 associated convective mixing. Owing to ground surface heating, the magnitude of
 326 vertical velocity varies seasonally, peaking in summer (~ 16 cm/s) and reaching its
 327 lowest in winter (~ -20 cm/s). This mountain-plain circulation directly affects the day
 328 and night difference in NH_3 concentrations at WTM throughout the year, following
 329 those variations.



330

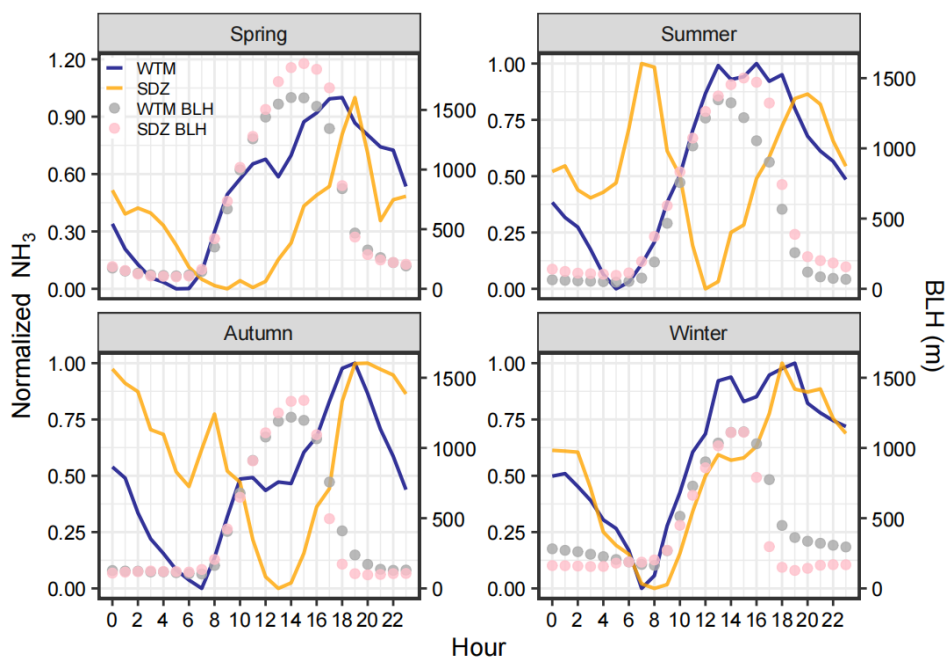
331 Fig. 5. Meridional cross-section of vertical velocity (contour region) with superimposed wind
 332 vectors. The yellow dotted lines represent the location of WTM. The four rows are the different
 333 seasons, including spring (a-b), summer (c-d), autumn (e-f), and winter (g-h).

334

3.4.2. Relationship between the diurnal variations of NH₃ and BLH

As mentioned in section 3.3, NCP, especially in the south of Hebei, the west of Shandong, and the east of Henan provinces, represents the shared common source area influencing WTM and SDZ. To figure out how the emissions emitted from this region affected two sites, diurnal variation of NH₃ and boundary layer height were analyzed (Fig. 6). In order to better illustrate the diurnal variation of NH₃ at these two sites more clearly, the normalized concentrations were applied. As shown in Fig. 6, NH₃ concentrations at SDZ didn't rise as the BLH elevated, except in winter. This might be due to the good dispersion and dilution conditions as the BLH increases that reduces the NH₃ levels. Since SDZ lies in the transitional zone between the NCP and the Mountain Yan area, it is primarily influenced by mountain-valley circulation (Lin et al., 2008). In the afternoon, under the impact of valley wind, lots of the pollutants from NCP were transported to SDZ by the southerly wind, leading to a peak concentration of NH₃ around 18:00 in seasons. However, apart from the late afternoon peak, morning spikes of NH₃ can also be found during summer and autumn. Based on previous studies, the morning NH₃ enhancement can be linked to dew evaporation since dew is a nighttime reservoir and morning source for NH₃ (Wentworth et al., 2016; Kuang et al., 2020).

However, different from the diurnal behavior of SDZ, NH₃ levels at WTM began to rise steadily around 8:00. During spring and autumn, peaks occurred around 18:00, while in winter and summer, peak durations were longer (12:00 – 18:00), followed by a rapid decline. It is particularly noteworthy that the diurnal variation of NH₃ concentration at WTM shows good consistency with the diurnal variation of BLH compared to SDZ, showing an increase in concentration as BLH rises and a decrease as BLH falls. This consistency might suggest that the mountain wind system transports the pollutants to the mountaintop during the day via upslope winds, along with the development of BLH through convective mixing. Conversely, nighttime downslope winds lead to the dispersion of these pollutants.



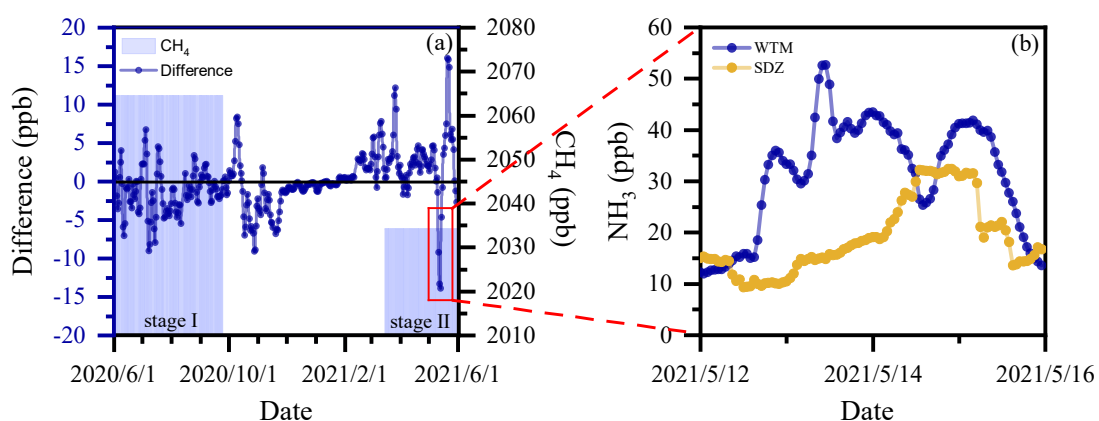
363
 364 Fig. 6. Diurnal variation of normalized NH_3 concentration and BLH at WTM (blue line and grey
 365 dots) and SDZ (orange line and pink dots), respectively.

366 However, despite the fact that the distance between WTM and SDZ is more than
 367 350 km and they are controlled by different transport patterns (i.e., mountain-plain and
 368 mountain-valley circulations in WTM and SDZ, respectively), their NH_3 levels still
 369 exhibit a high similarity. To find out the underlying factor driving this convergence,
 370 CH_4 data at SDZ was used to explain.

371 Fig. 7a presents the variations in the NH_3 concentration difference between SDZ
 372 and WTM, along with the average CH_4 concentration across different periods. During
 373 Stage I (summer to early autumn), the fluctuation of the NH_3 concentration difference
 374 is relatively small, ranging approximately from -5 to 5 ppb. In contrast, during Stage II
 375 (spring), the fluctuation amplitude of the difference increases significantly, and the
 376 values are mostly positive except for the period from May 12 to May 15, 2021 (Fig.
 377 7b), indicating that the NH_3 concentration at SDZ is higher than that at WTM during
 378 this period. Corresponding to these patterns, the CH_4 concentration at SDZ is higher in
 379 stage I and lower in stage II.

380 As CH_4 is a key indicator of agricultural emissions, and the CH_4 concentration at
 381 SDZ can represent the background level of agricultural emissions in North China, the
 382 relationship between the NH_3 concentration difference and CH_4 levels in stages I and II

383 can be interpreted as follows: during stage I, when regional agricultural emissions are
 384 strong, the NH_3 concentrations at WTM and SDZ are more closely aligned, reflecting
 385 the dominant role of agricultural sources in homogenizing the concentrations at the two
 386 sites. Conversely, during stage II, when regional agricultural emissions are weak, the
 387 NH_3 concentration at SDZ is significantly affected by emissions from urban Beijing
 388 due to the transport of southerly winds. This leads to a larger concentration difference
 389 between the two sites, while the lower CH_4 concentration at SDZ further confirms the
 390 reduced influence of agricultural sources during this period.



391
 392 Fig. 7. Time series of average CH_4 concentration at SDZ and daily concentration difference between
 393 SDZ and WTM (a) and hourly concentration at each site (b).

394 3.4.3. A typical case simulation

395 To find out why NH_3 at WTM exhibited a higher level than that at SDZ in stage II,
 396 a typical case of May 12, 2021, was simulated to more clearly illustrate how NH_3
 397 concentration varies with the evolution of the wind field and BLH at WTM. Fig. S4
 398 shows the simulated and observed hourly mean NH_3 concentration, WD, and WS at the
 399 WTM and SDZ on 12 May, 2021. Although the model has evident deviations in
 400 simulating the concentration values, it accurately captures the diurnal variations in NH_3
 401 levels and surface wind fields at both stations. Consequently, the simulation results are
 402 deemed reliable for further analysis of transport characteristics.

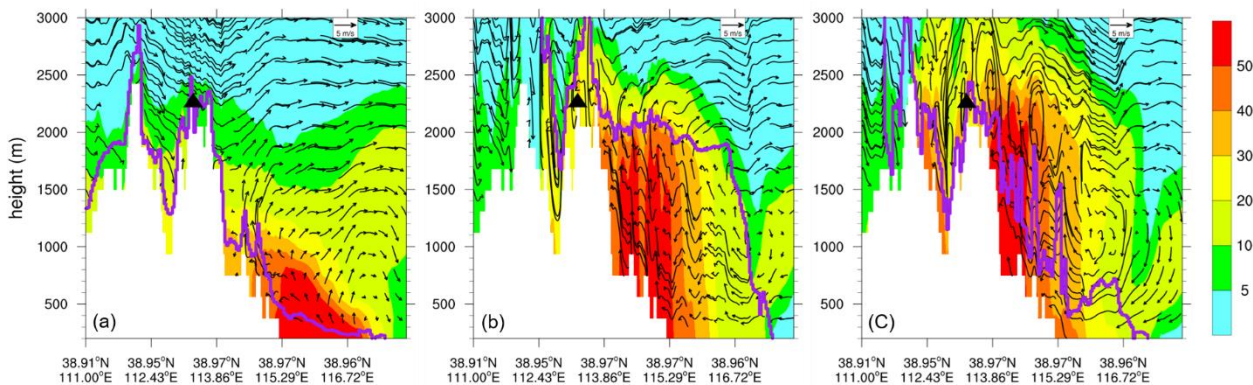
403 As shown in Fig. S4, on May 12, 2021, the prevailing wind direction in the NCP
 404 region was southeast, with a strong east wind system traversing the mountainous areas
 405 west of the NCP. NH_3 concentration exhibited a transport pattern from the eastern plain

406 to the western mountains, significantly impacting the WTM. During this period, the air
407 mass affecting the SDZ station mainly originated from the Bohai Sea area, with no
408 significant pollutant transport from the NCP, thus maintaining consistently low NH_3
409 levels (Fig. S4a).

410 In addition to the transport effect of the southeasterly wind in the horizontal
411 direction, the lifting of the boundary layer height also plays a crucial role in the increase
412 in NH_3 concentration at the WTM station. To more finely illustrate the process of NH_3
413 concentration varying with the evolution of wind fields and boundary layer height, an
414 east-to-west cross section (shown in Fig. S4b) has been selected for detailed analysis.
415 As shown in Fig. 8, although similarly affected by the easterly wind, the NH_3 emitted
416 from the plain area on the morning of May 12 was trapped in the plain area due to the
417 lower BLH, resulting in low concentrations at the WTM (Fig. 8a). In the afternoon, air
418 masses with higher NH_3 levels from the eastern plain region rise upward with the
419 increase of BLH and are simultaneously pushed up along the slope by the prevailing
420 easterly winds within the boundary layer, gradually affecting the WTM area (Fig. 8b).
421 At the same time, both observations and simulations at WTM showed a rapid increase
422 in ground-level NH_3 concentrations (Fig. S4a). After nightfall, this high concentration
423 situation persisted at WTM in the absence of strong weather systems (Fig. 8c). Our
424 simulation result validates the aforementioned analysis that anthropogenic emissions
425 from NCP, influenced by the regional transport and boundary layer lifting, would lead
426 to an increase in NH_3 levels in the relatively distant mountain areas with high altitude.

427 It is noteworthy that the modeling study of the typical case on 12 May 2021 was
428 designed to corroborate the analysis based on observational data and to qualitatively
429 elucidate the horizontal and vertical transport pathways of NH_3 , as well as their
430 relationship with boundary layer dynamics. However, the simulation results have
431 limitations in accurately capturing NH_3 concentrations within a regional area and in the
432 quantitative assessment of transport impacts. These aspects will be the focus of further
433 investigation in future work.

434



441

442 Fig. 8. West–east vertical distributions of NH_3 mixing ratios (ppb) and vertical wind velocity (cm
 443 s^{-1}) at (a) 08:00 LST, (b) 16:00 LST, and (c) 19:00 LST on 12 May 2021. Note that vertical velocities
 444 are scaled by a factor of 100 in the wind vectors. The cross-section location is indicated by the solid
 445 black line in Fig. S4b. Wind vectors are overlaid on the NH_3 distributions. The thick purple curves
 446 denote the top of the atmospheric boundary layer. The approximate location of the WTM site
 447 is marked with a black triangle.

448

449 4. Conclusion

450 Continuous high-resolution and real-time NH_3 observations made from Jun 1,
 451 2020 to May 31, 2021 were simultaneously conducted at WTM, SDZ, and BMS. The
 452 average concentration of NH_3 at WTM was 9.0 ± 6.7 ppb during the study period.
 453 Compared to the same type of observation site in previous studies (e.g., forest or
 454 grassland mountain sites), the NH_3 concentration measured at WTM was much higher
 455 than those reported by Pan et al. (2018), Ban et al. (2016), and Benedict et al. (2013).
 456 On the other hand, although WTM is located in a remote area, its NH_3 levels were very
 457 close to those at the background station (SDZ) in the northern edge of NCP, while being
 458 much lower than those at the megacity station (BMS) in NCP. To identify the primary
 459 factors driving the similarity in NH_3 levels between WTM and SDZ, meteorological
 460 effects, potential source regions, and transport patterns were analyzed.

461 CCM analysis between NH_3 and meteorological variables revealed that WD, WS,
 462 and BLH significantly regulate NH_3 levels at both WTM and SDZ across all seasons.
 463 The relationships of wind and NH_3 concentration as well as PSCF results suggested that
 464 these sites were influenced by a shared common source area in the NCP, especially in
 465 the south of Hebei, the west of Shandong, and the east of Henan provinces.

466 The influence of pollutants emitted from NCP on WTM and SDZ was different.

467 NH₃ concentrations at SDZ were primarily controlled by the mountain-valley
468 circulation, which could transport the NH₃ from NCP to it by valley wind. For WTM,
469 under the effect of mountain-plain circulation and the diurnal variation of BLH, the
470 pollutant from NCP was carried up to the top of the mountain by the vertical transport
471 and convective mixing. This transport pattern was further confirmed by WRF-Chem
472 simulation.

473 Furthermore, the correlation between CH₄ concentrations and the NH₃ level
474 difference between SDZ and WTM indicated that regional agricultural emissions in
475 NCP were the dominant factor contributing to the NH₃ similarity between these two
476 sites – even though the two sites differed significantly in altitude and geography.

477 Our study provides a full annual cycle of measurements at a location that is
478 underrepresented in the global ammonia monitoring network, and highlights that
479 emissions from the NCP can influence NH₃ concentrations at both high-altitude and
480 background areas in northern China by different transport mechanisms. These results
481 could help policymakers develop effective strategies for mitigating regional air
482 pollution. However, our results cannot distinguish specific NH₃ sources and their
483 quantitative contributions. Therefore, additional $\delta^{15}\text{N}$ isotope measurements are needed
484 in future studies.

485

486 **Data availability.**

487 The data are available at <https://zenodo.org/records/17089450> (Pu et al., 2025)

488

489 **Competing interests.**

490 The authors declare that none of the authors has any competing interests.

491

492 **Author contributions.**

493 WP analyzed the data and prepared the manuscript. JX revised the manuscript. LZ
494 and JD conducted the measurements. ZM supervised the project. All co-authors
495 discussed the results and commented on the manuscript.

496

497 **Acknowledgements.**

498 The authors would like to acknowledge the Beijing Meteorological Information
499 Center for supporting the meteorological data collection.

500

501 **Financial support.**

502 This work was supported by the National Natural Science Foundation of China
503 (Grant No. 42275188, No. 42005094, No.42177091).

504

505 **References:**

506 Baek, B. H., Aneja, V. P. J. J. o. t. A., and Association, W. M.: Measurement and analysis of the
507 relationship between ammonia, acid gases, and fine particles in eastern North Carolina, 54, 623-
508 633, 2004.

509 Chen, Z., Xu, M., Gao, B., Sugihara, G., Shen, F., Cai, Y., Li, A., Wu, Q., Yang, L., Yao, Q., Chen, X.,
510 Yang, J., Zhou, C., and Li, M.: Causation inference in complicated atmospheric environment,
511 Environmental Pollution, 303, 119057, <https://doi.org/10.1016/j.envpol.2022.119057>, 2022.

512 Chen, Z., Chen, D., Zhao, C., Kwan, M.-p., Cai, J., Zhuang, Y., Zhao, B., Wang, X., Chen, B., Yang, J.,
513 Li, R., He, B., Gao, B., Wang, K., and Xu, B.: Influence of meteorological conditions on PM2.5
514 concentrations across China: A review of methodology and mechanism, Environment International,
515 139, 105558, <https://doi.org/10.1016/j.envint.2020.105558>, 2020.

516 Clark, A. T., Ye, H., Isbell, F., Deyle, E. R., and Sugihara, G. J. E.: Spatial 'convergent cross mapping'
517 to detect causal relationships from short time-series, 96, 1174, 2015.

518 Dammers, E., McLinden, C. A., Griffin, D., Shephard, M. W., Van Der Graaf, S., Lutsch, E., Schaap,
519 M., Gainairu-Matz, Y., Fioletov, V., Van Damme, M., Whitburn, S., Clarisse, L., Cady-Pereira, K.,
520 Clerbaux, C., Coheur, P. F., and Erisman, J. W.: NH₃ emissions from large point sources derived
521 from CrIS and IASI satellite observations, Atmos. Chem. Phys., 19, 12261-12293, 10.5194/acp-19-
522 12261-2019, 2019.

523 Elser, M., El-Haddad, I., Maasikmets, M., Bozzetti, C., Wolf, R., Ciarelli, G., Slowik, J. G., Richter, R.,
524 Teinmaa, E., Hüglin, C., Baltensperger, U., and Prévôt, A. S. H.: High contributions of vehicular
525 emissions to ammonia in three European cities derived from mobile measurements, Atmospheric
526 Environment, 175, 210-220, <https://doi.org/10.1016/j.atmosenv.2017.11.030>, 2018.

527 Giorgino, T. J. J. o. S. S.: Computing and Visualizing Dynamic Time Warping Alignments in R: The
528 dtw Package, 031, 2009.

529 Grell, G. A., Peckham, S. E., Schmitz, R., McKeen, S. A., Frost, G., Skamarock, W. C., and Eder, B.:
530 Fully coupled "online" chemistry within the WRF model, Atmospheric Environment, 39, 6957-6975,
531 <https://doi.org/10.1016/j.atmosenv.2005.04.027>, 2005.

532 Höpfner, M., Volkamer, R., Grabowski, U., Grutter, M., Orphal, J., Stiller, G., von Clarmann, T., and
533 Wetzell, G.: First detection of ammonia (NH₃) in the Asian summer monsoon upper troposphere,
534 Atmos. Chem. Phys., 16, 14357-14369, 10.5194/acp-16-14357-2016, 2016.

535 Kuang, Y., Xu, W., Lin, W., Meng, Z., Zhao, H., Ren, S., Zhang, G., Liang, L., and Xu, X.: Explosive
536 morning growth phenomena of NH₃ on the North China Plain: Causes and potential impacts on
537 aerosol formation, Environmental Pollution, 257, 113621,

538 <https://doi.org/10.1016/j.envpol.2019.113621>, 2020.

539 Lan, Z., Lin, W., Pu, W., Ma, Z. J. A. C., and Physics: Measurement report: Exploring NH₃ behavior
540 in urban and suburban Beijing: comparison and implications, 2021.

541 Leen, J. B., Yu, X.-Y., Gupta, M., Baer, D. S., Hubbe, J. M., Kluzek, C. D., Tomlinson, J. M., and Hubbell,
542 M. R., II: Fast In Situ Airborne Measurement of Ammonia Using a Mid-Infrared Off-Axis ICOS
543 Spectrometer, *Environmental Science & Technology*, 47, 10446-10453, 10.1021/es401134u, 2013.

544 Li, B., Chen, L., Shen, W., Jin, J., Wang, T., Wang, P., Yang, Y., and Liao, H.: Improved gridded
545 ammonia emission inventory in China, *Atmos. Chem. Phys.*, 21, 15883-15900, 10.5194/acp-21-
546 15883-2021, 2021.

547 Li, Y., Thompson, T. M., Van Damme, M., Chen, X., Benedict, K. B., Shao, Y., Day, D., Boris, A., Sullivan,
548 A. P., Ham, J. J. A. C., and Physics: Temporal and spatial variability of ammonia in urban and
549 agricultural regions of northern Colorado, United States, 17, 1-50, 2017.

550 Lin, W., Xu, X., Zhang, X., Tang, J. J. A. C., and Physics: Contributions of pollutants from North China
551 Plain to surface ozone at the Shangdianzi GAW Station, 8, 2008.

552 Liu, M., Huang, X., Song, Y., Tang, J., Cao, J., Zhang, X., Zhang, Q., Wang, S., Xu, T., Kang, L., Cai, X.,
553 Zhang, H., Yang, F., Wang, H., Yu, J. Z., Lau, A. K. H., He, L., Huang, X., Duan, L., Ding, A., Xue, L.,
554 Gao, J., Liu, B., and Zhu, T.: Ammonia emission control in China would mitigate haze pollution and
555 nitrogen deposition, but worsen acid rain, 116, 7760-7765, 10.1073/pnas.1814880116, 2019.

556 Nowak, J. B., Neuman, J. A., Bahreini, R., Middlebrook, A. M., Holloway, J. S., McKeen, S. A., Parrish,
557 D. D., Ryerson, T. B., and Trainer, M.: Ammonia sources in the California South Coast Air Basin and
558 their impact on ammonium nitrate formation, 39, <https://doi.org/10.1029/2012GL051197>, 2012.

559 Nowak, J. B., Neuman, J. A., Bahreini, R., Brock, C. A., Middlebrook, A. M., Wollny, A. G., Holloway,
560 J. S., Peischl, J., Ryerson, T. B., and Fehsenfeld, F. C.: Airborne observations of ammonia and
561 ammonium nitrate formation over Houston, Texas, 115, <https://doi.org/10.1029/2010JD014195>,
562 2010.

563 Nowak, J. B., Neuman, J. A., Kozai, K., Huey, L. G., Tanner, D. J., Holloway, J. S., Ryerson, T. B., Frost,
564 G. J., McKeen, S. A., and Fehsenfeld, F. C.: A chemical ionization mass spectrometry technique for
565 airborne measurements of ammonia, 112, <https://doi.org/10.1029/2006JD007589>, 2007.

566 Pu, W., Guo, H., Ma, Z., Qiu, Y., Tang, Y., Liu, Q., Wang, F., and Sheng, J.: Aircraft measurements
567 reveal vertical distribution of atmospheric ammonia over the North China Plain in early autumn,
568 *Environmental Chemistry Letters*, 18, 2149-2156, 10.1007/s10311-020-01051-4, 2020a.

569 Pu, W., Ma, Z., Collett Jr, J. L., Guo, H., Lin, W., Cheng, Y., Quan, W., Li, Y., Dong, F., and He, D.:
570 Regional transport and urban emissions are important ammonia contributors in Beijing, China,
571 *Environmental Pollution*, 265, 115062, <https://doi.org/10.1016/j.envpol.2020.115062>, 2020b.

572 Pu, W., Sheng, J., Tian, P., Huang, M., Liu, X., Collett, J. L., Li, Z., Zhao, X., He, D., Dong, F., Zhang,
573 N., Quan, W., Qiu, Y., Song, Y., Lin, W., Pan, Y., and Ma, Z.: On-road mobile mapping of spatial
574 variations and source contributions of ammonia in Beijing, China, *Science of The Total
575 Environment*, 864, 160869, <https://doi.org/10.1016/j.scitotenv.2022.160869>, 2023.

576 Rawat, V., Singh, N., Singh, J., Rajput, A., Dhaka, S. K., Matsumi, Y., Nakayama, T., and Hayashida,
577 S.: Assessing the high-resolution PM_{2.5} measurements over a Central Himalayan site: impact of
578 mountain meteorology and episodic events, *Air Quality, Atmosphere & Health*, 17, 51-70,
579 10.1007/s11869-023-01429-7, 2024.

580 Schiferl, L. D., Heald, C. L., Van Damme, M., Clarisse, L., Clerbaux, C., Coheur, P. F., Nowak, J. B.,
581 Neuman, J. A., Herndon, S. C., Roscioli, J. R., and Eilerman, S. J.: Interannual variability of ammonia

582 concentrations over the United States: sources and implications, *Atmos. Chem. Phys.*, 16, 12305-
583 12328, 10.5194/acp-16-12305-2016, 2016.

584 Shephard, M. W., Cady-Pereira, K. E., Luo, M., Henze, D. K., Pinder, R. W., Walker, J. T., Rinsland, C.
585 P., Bash, J. O., Zhu, L., Payne, V. H. J. A. C., and Physics: TES ammonia retrieval strategy and global
586 observations of the spatial and seasonal variability of ammonia, 11, 10743-10763, 2011.

587 Sugihara, G., May, R., Ye, H., Hsieh, C.-h., Deyle, E., Fogarty, M., and Munch, S.: Detecting Causality
588 in Complex Ecosystems, 338, 496-500, doi:10.1126/science.1227079, 2012.

589 Van Damme, M., Clarisse, L., Whitburn, S., Hadji-Lazaro, J., Hurtmans, D., Clerbaux, C., and Coheur,
590 P.-F.: Industrial and agricultural ammonia point sources exposed, *Nature*, 564, 99-103,
591 10.1038/s41586-018-0747-1, 2018.

592 Van Damme, M., Clarisse, L., Heald, C. L., Hurtmans, D., Ngadi, Y., Clerbaux, C., Dolman, A. J.,
593 Erisman, J. W., and Coheur, P. F.: Global distributions, time series and error characterization of
594 atmospheric ammonia (NH₃) from IASI satellite observations, *Atmos. Chem. Phys.*,
595 14, 2905-2922, 10.5194/acp-14-2905-2014, 2014.

596 Warner, J. X., Dickerson, R. R., Wei, Z., Strow, L. L., Wang, Y., and Liang, Q. J. G. R. L.: Increased
597 atmospheric ammonia over the world's major agricultural areas detected from space, 44, 2875-
598 2884, 2017.

599 Warner, J. X., Wei, Z., Strow, L. L., Dickerson, R. R., Nowak, J. B. J. A. C., and Physics: The global
600 tropospheric ammonia distribution as seen in the 13 year AIRS measurement record, 15, 35823-
601 35856, 2015.

602 Wentworth, G. R., Murphy, J. G., Benedict, K. B., Bangs, E. J., Jr, J. L. C. J. A. C., and Physics: The role
603 of dew as a night-time reservoir and morning source for atmospheric ammonia, 16, 1-36, 2016.

604 Wiedinmyer, C., Akagi, S. K., Yokelson, R. J., Emmons, L. K., Al-Saadi, J. A., Orlando, J. J., and Soja,
605 A. J.: The Fire INventory from NCAR (FINN): a high resolution global model to estimate the
606 emissions from open burning, *Geosci. Model Dev.*, 4, 625-641, 10.5194/gmd-4-625-2011, 2011.

607 Xu, L., Penner, J. J. A. c., and Physics: Global simulations of nitrate and ammonium aerosols and
608 their radiative effects, 12, 9479-9504, 2012.

609 Zaveri, R. A. and Peters, L. K. J. J. o. G. R. A.: A new lumped structure photochemical mechanism
610 for large-scale applications, 104, 1999.

611 Zhang, G., Yan, H., Li, T., Zhu, Y., Zhou, S., Feng, Y., and Zhou, W.: Relation analysis on emission
612 control and economic cost of SCR system for marine diesels, *Science of The Total Environment*,
613 788, 147856, <https://doi.org/10.1016/j.scitotenv.2021.147856>, 2021.

614 Zhang, Q., Streets, D. G., Carmichael, G. R., He, K., Huo, H., Kannari, A., Klimont, Z., Park, I., Reddy,
615 S., Fu, J. S. J. A. C., and Discussions, P.: Asian emissions in 2006 for the NASA INTEX-B mission,
616 2009.

617 Zhang, Y., Ma, X., Tang, A., Fang, Y., Misselbrook, T., and Liu, X.: Source Apportionment of
618 Atmospheric Ammonia at 16 Sites in China Using a Bayesian Isotope Mixing Model Based on
619 $\delta^{15}\text{N-NH}_x$ Signatures, *Environmental Science & Technology*, 57, 6599-6608,
620 10.1021/acs.est.2c09796, 2023.

621 Zhang, Y., Tang, A., Wang, D., Wang, Q., Benedict, K., Zhang, L., Liu, D., Li, Y., Collett Jr, J. L., Sun,
622 Y., and Liu, X.: The vertical variability of ammonia in urban Beijing, China, *Atmos. Chem. Phys.*, 18,
623 16385-16398, 10.5194/acp-18-16385-2018, 2018.

624 Ziyue, C., Xiaoming, X., Jun, C., Danlu, C., Bingbo, G., Bin, H., Nianliang, C., Bing, X. J. A. C., and
625 Discussions, P.: Understanding meteorological influences on PM_{2.5} concentrations across China:

- 626 a temporal and spatial perspective, 1-30, 2018.
- 627 Pu, W., Xu, J., Zhu, L., Liu, C., Zhou, L., Dong, J., Ge, S., Ma, Z.: Hourly measurement dataset of
- 628 ammonia, Zenodo [Data set], <https://zenodo.org/records/17089450>, 2025.